CCFE
CULHAM CENTRE FOR FUSION ENERGY

UK Atomic Energy Authority

UKAEA-CCFE-PR(19)31

George Fulton, Artem Lunev

Probing the correlation between phase evolution and growth kinetics in the oxide layers of tungsten using Raman spectroscopy and EBSD

Probing the correlation between phase evolution and growth kinetics in the oxide layers of tungsten using Raman spectroscopy and EBSD

George Fulton, Artem Lunev

This is a preprint of a paper submitted for publication in Corrosion Science

Development of tungsten oxides on {1 1 1} and {0 0 1} crystallographic planes in hot-rolled tungsten

George Fulton*, Artem Lunev*

United Kingdom Atomic Energy Authority (UKAEA), Culham Science Centre, Abingdon, Oxfordshire OX14 3DB, United Kingdom

Abstract

Tungsten, a material for the high heat flux components of fusion reactors, may be exposed to air as a result of abnormal operation or accidents. Little is known about oxidation mechanisms in this material at micro-scale due to the complexity of characterisation. This work addresses the crystallographic dependence of oxidation in hot-rolled Plansee tungsten. Anneals in Ar–O_2 at a temperature $T = 400$ °C have been carried out at different oxygen partial pressures and oxidation times to study the initiation and progression of oxidation. A combination of electron back-scattering diffraction (EBSD), Raman scattering analysis, and confocal laser scanning microscopy (CLSM) shows preferential oxidation on {1 1 1} tungsten planes, which later reverses to {0 0 1} planes. A novel statistically-driven approach is taken to analyse the occurrence of oxide phases. It is shown that the orthorhombic (o–WO_3) and the hexagonal (h–WO_3) tungsten trioxides may precipitate simultaneously on different crystallographic planes at the base material surface.

Keywords: A. tungsten; B. Raman spectroscopy; B. EBSD; B. CLSM; C. oxidation

*These authors have contributed equally. Authors names are listed in alphabetic order.
Email address: artem.lunev@ukaea.uk (Artem Lunev)

1. Introduction

Tungsten, a refractory BCC metal with high thermal conductivity [1] and low sputtering yield [2, 3, 4], is the current material of choice for the divertor component of International Thermonuclear Reactor (ITER) [5, 6] – and potentially for the DEMOnstration Power Station. There are two major issues with using tungsten as a divertor material. Firstly, the low oxidation resistance [7, 8] of ITER grade (99.94 wt. % fully sintered; forged and/or swaged, cold or/and hot-rolled and stress relieved [9]) tungsten involves certain risks during accidents and abnormal operation (such as air leaks [10]). A worst case loss-of-coolant accident (LOCA) scenario with simultaneous air ingress [11, 12] would result in a complete loss of the tungsten monoblock divertor by its conversion to volatile oxides [13]. In the absence of cooling, nuclear decay heat would gradually increase the divertor temperature beyond the point at which oxides start to volatilise. These oxides contain radioactive material formed during reactor operation [13]. The second issue pertaining to the use of tungsten in fusion applications is its high brittle-to-ductile transition temperature [2, 14], which may lead to cracking during high thermal loads in the event of plasma disruption.

Multiple attempts have been undertaken to promote oxidation resistance of tungsten-based materials by proposing several ternary (W–Cr–Y 'smart alloys' [15, 16, 17]) and quaternary (W–Mo–Cr–Pd [18, 19, 20]) tungsten alloys. Although some results look promising, the new material is still unlikely to withstand an extended LOCA event, which could last for up to three months. For instance, the passivating Cr_2O_3 layer in a W-Cr-Y smart alloy is breached after 467 h oxidation at 1000 °C [21]. With increasing the complexity of composition, it becomes harder to predict how other properties of these alloys (e.g., thermal conductivity, fracture toughness) will evolve, and whether the original benefits of using tungsten are preserved. Another trend in tungsten alloy design places emphasis on improving mechanical properties of the base material and considers a completely separate set of alloying elements (potassium, rhenium, lanthanum oxide [22]). These two lines of thought may potentially be conflicting.

A systematic study of tungsten oxidation is still lacking, although many researchers have proposed different interesting approaches to tackle this phenomenon [23, 8, 24, 25]. For instance, analysis of tungsten exposed to short oxidation at small oxygen partial pressure has been previously reported in [23, 25]. Authors of [24, 25] have observed preferential oxidation in tungsten (Schlueter & Balden [24] report preferential oxidation on {0 0 1} grains) when the average thickness of the oxide layer is about a few micrometers – an effect known in zirconium alloys for fuel cladding materials in fission reactors [26] and some silver-based intermetallic compounds [27]. Cifuentes et al. [8] report different oxide phases found on the surface of tungsten oxidised at 600–800 °C for up to 100 h. Overall, the tungsten-oxygen system seems to be a very complex one. A variety of oxides may be formed on the surface of pure tungsten including [28, 29]: stable stoichiometric oxides formed by either W^{4+}, W^{5+}, or W^{6+} ions; non-stoichiometric oxides formed by a mix of different ion species; metastable oxides with intermediate compositions presented by W_nO_{3n-2} and W_nO_{3n-1} series, also known as the homologous Magneli phases. In addition, tungsten trioxide (WO_3), which is also the higher oxide in this system, comes in variety of polymorphous states, including: monoclinic, triclinic, tetragonal, hexagonal, and orthorhombic. This material attracts significant attention due to its unique semiconducting properties [30, 31].

The goal of this study is to examine how the crystallographic orientation of tungsten grains affects the oxidation process – both at the initial stage, when the oxide scale is very thin and oxidation is mainly controlled by adsorption, and at later stages, when the growth of the oxide is mostly diffusion-controlled.

2. Material and methods

2.1. Sample preparation

Cylindrical (⌀ 3 mm × 0.5 mm) samples were cut by electrical discharge machining from standard quality, hot-rolled pickled 99.97 wt. % pure tungsten sheet (1 mm × 100 mm × 100 mm) supplied by Plansee.

Grinding and polishing was performed using an AutoMet™ 250 Grinder-Polisher. For this purpose, samples were mounted on stainless steel holders with Crystalbond™ 509. Wet grinding was done with SiC paper followed by fine polishing with 3 μm and 1 μm diamond suspension. The final stage of polishing involved using Buehler MasterMet 2 Non-Crystallizing Colloidal Silica. To ensure samples were free of scratches, examination on an Olympus MX51 optical microscope was performed between polishing stages. Samples were thoroughly rinsed with water to avoid colloidal silica stains. Crystal bond was removed with acetone in an ultra-sonic bath. Residues of acetone and carbon contamination were removed from the samples' surface by rinsing in isopropanol and deionised water and scrubbing with PELCO optical lens tissue until no carbon particles could be observed with low-magnification optical microscopy.

Samples were subsequently mounted on double-sided conductive adhesive copper tape. For later imaging analysis, three fiducial markers (≈ 10 μm each) – to introduce asymmetry used for orienting the sample – were indented on each sample (Fig. 1). This was done using a Agilent Nanoindenter G200 in the indentation mode with a Berkovich tip.

Finally, before oxidation experiments, the copper tape was removed and samples were cleaned to remove residual adhesive following the cleaning procedure above. Cleaned or oxidised samples were kept in a desiccator system at near vacuum.

2.2. Characterisation methods

Prior to oxidation, samples were characterised with SEM and electron back scattered diffraction (EBSD). In addition, large-area (350 μm $\times$ 350 μm) scans were performed with confocal laser scanning microscopy (CLSM) to gather data on surface roughness. Raman spectroscopy and CLSM imaging were used to examine the oxidised layer.

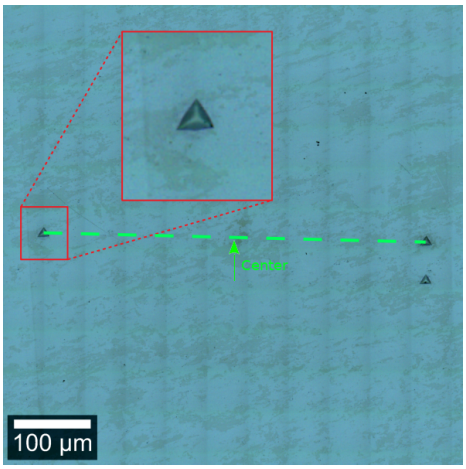

Figure 1: Stitching of optical images (×50) showing asymmetric fiducial markers introduced for orientation on a sample. The reference point is chosen as the middle point of the segment connecting two upper indents and also coincides with the geometric center of the sample.

2.2.1. SEM and EBSD

The SEM used in this work was TESCAN Mira3 XMH with a Schottky field emission gun and a NordlysNano EBSD detector. For EBSD mapping (Fig. 2) samples were placed on a 70° pre-tilted specimen holder. The following settings were used during imaging: high voltage (HV) 20 kV, DEPTH scanning mode and beam intensity ≈ 20 (corresponding to a spot size 60–70 nm). Samples were oriented so that indents were aligned vertically (as in Fig. 1). For EBSD, the scan region was centered exactly between the indents. After centering, the view field was set to 550 μm, and the size of the scan region inside that view field was set to 350 μm × 350 μm. A step size of 0.25–0.34 μm was chosen for EBSD imaging to allow detailed mapping. Due to the tilt and long scanning time (2 hours), samples experienced small drift, which was corrected for using the Aztec automatic drift correction. For Kikuchi pattern acquisition, we used a gain of 5–7, exposure time of 20–35 ms, and binning mode 4×4. The percentage of unresolved pixels was less than 10 %, which allowed effective noise elimination using HKL CHANNEL5 post-processing software (9×9 smoothing window). For grain boundary detection, the critical angle was set to 10° and minimum grain

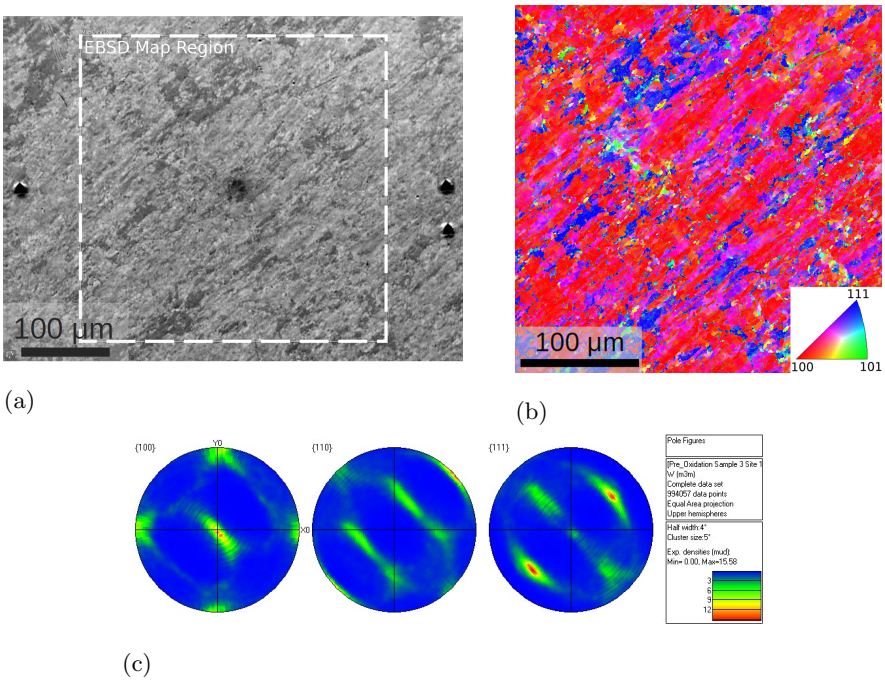

Figure 2: Crystallographic texture of as-prepared samples: (a) Mixed secondary electrons (SE) and front scattering detector (FSD) image showing topography variation on as-prepared samples. The rectangular area shows the EBSD scan region (b) The unprocessed EBSD inverse pole figure (IPF) z map, with z axis orthogonal to the surface; (c) $\{0\,0\,1\}$, $(1\,1\,0)$, $\{1\,1\,1\}$ pole figures showing the complete texture information.

size to 10 pixels.

2.2.2. Raman spectroscopy and CLSM

Raman spectroscopy has been used recently to characterise structural changes in nanocrystalline WO_3 as a function of applied voltage [32], and to characterise thin (up to 200 nm) oxide layer formed on a tungsten metal before and after exposure to deuterium or helium plasma [33, 34]. CLSM has been used previously as a tool to study topography in the range of 1–2 μm in oxidized and sputtered tungsten in [24, 4].

In this work, the WITec alpha300 R confocal Raman imaging microscope was used to acquire Raman spectra in the raster mode and perform large area

scans (Raman and CLSM maps). The TrueSurface feature enabled dynamic focusing of the confocal laser during scanning. The inter-quartile (IQR) range of CLSM data gathered from the 350 μm $\times$ 350 μm (pixel size 250 px $\times$ 250 px) region, centered as shown in Fig. 1 using the piezo-motors of the scanning stage was used to characterise the pre-oxidised surface topography. Post-oxidation confocal mapping in combination with the Raman spectroscopy were carried out on 75 μm $\times$ 75 μm (pixel size 1500 px $\times$ 1500 px) areas. For individual Raman spectra a conventional low-noise high-intensity detection mode was used (integration time was set to 0.5 s with 100–300 accumulations); whereas for the large area scans (75 μm $\times$ 75 μm) an electron multiplying charge coupled device (EMCCD) camera was selected which allowed fast acquisition (scanning time $\approx$ 2 h per sample). The latter could be achieved by adopting a gain of 230 and an integration time of 1×10^{-5} s using this specialist detector. For all samples, a green laser (531.95 nm) and a 1800 g/mm grating were used. The laser power was kept below 3 mW to avoid permanent damage to the W oxide surface.

2.3. Data processing methods

Raman spectroscopy is based on the inelastic scattering of photons. In this process, the material under test (MUT) is polarised by an incoming photon of any frequency, generating a virtual excited energy state. If a change in vibrational state of the MUT induces a change in polarisation, then the energy of the re-radiated photon is shifted. This shift in energy can be measured and is known as Raman scattering. However, this process is very inefficient and non-resonant. On the other hand, fluorescence caused by the excitation of MUT electronic states, is a highly efficient, resonant process. Therefore, accumulated Raman spectra suffer from a superimposed baseline signal caused by fluorescence and for low laser powers, are sensitive to noise. Both smoothing to remove noise and a baseline subtraction are required to access the underlying Raman signal, which contains the material bond-specific characteristic vibrational energies.

2.3.1. Smoothing based on LOESS filter with BIC statistic

In order to remove noise from the baseline Raman signal, a locally estimated scatterplot smoothing (LOESS) filter [35] is used. This LOESS algorithm has one parameter, the window size, which sets the smoothing region. For each window, a second order polynomial is fitted via a standard least squares regression with no weighting term. The ideal window size or number of windows was calculated by using the Bayesian Information Criterion (BIC). In this approach, the sum of least squares is penalised by an additional term which is weighted by the parameter k. The BIC statistic is then defined as:

$$\mathrm{BIC} = n \log \sigma_e^2 + k \log n \tag{1}$$

where n is the number of measured points, σ_e^2 is the mean square error and k is the number of parameters.

The number of windows, m is directly proportional to this penalisation factor k. The coefficient of proportionality is equal to 4, arising from the 3 variables $(\theta_0, \theta_1, \theta_2)$ required for second order polynomial fitting and the additional variance term. An example of this fitting is shown in Fig. 3.

2.3.2. Baseline subtraction based on asymmetric least squares smoothing

In order to remove the superimposed baseline from the Raman signal, an asymmetric least squares (AsLS) approach is taken [36]. This fitting procedure relies on two parameters: λ and p. λ is the curvature penalisation term, and p determines the asymmetry in the least squares iterations:

$$S = \sum_i^n w_i (y_i - z_i)^2 + \lambda \sum_i^n (\Delta^2 z_i) \tag{2}$$

where $w_i = p$, if $y_i > z_i$, else $w_i = (1 - p)$. Typically $\lambda = 10^5$ – 10^7 and $p = 0.001$ – 0.05.

The AsLS is encoded in the weighting term w_i. If the calculated baseline intensity z_i is higher than the measured signal, then the weighting term is equal to $(1-p)$ and is large. A set of linear equations is solved iteratively in reference to [37]. Fig. 3c illustrates the baseline fitting procedure for a model spectrum.

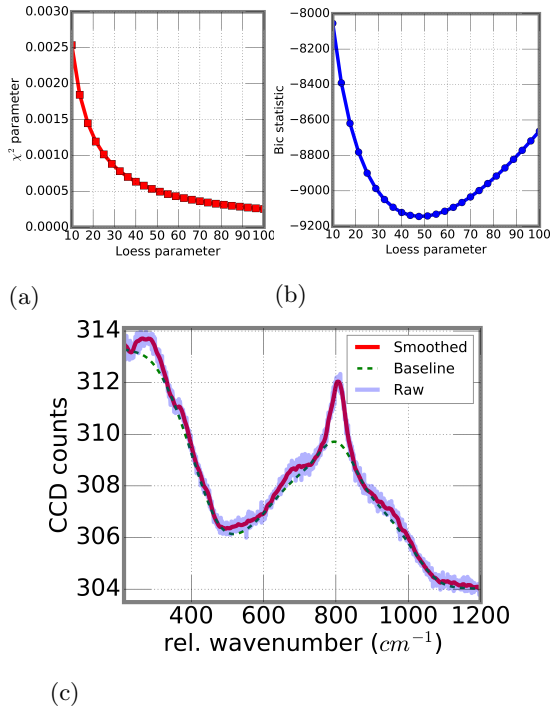

Figure 3: LOESS filter smoothing of W oxide Raman spectra: (a) Mean squared error (MSE) variation with loess window number; (b) Bayesian information criterion (BIC) variation with LOESS window number; (c) Resulting smoothed W oxide Raman spectra calculated with a LOESS window size given by the local minima in (b). The baseline is calculated using the asymmetric least squares (AsLS) fitting procedure.

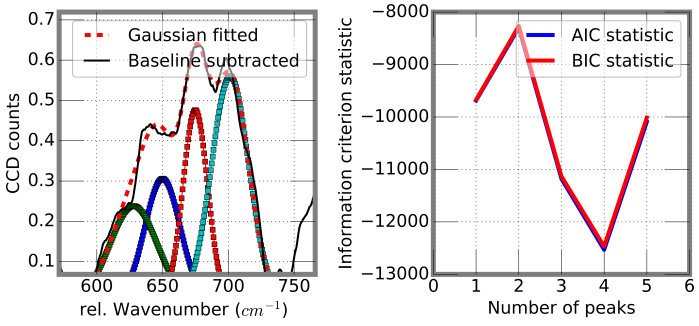

Figure 4: Gaussian deconvolution based on Levenberg-Marquardt damped least-squares (DLS) on model W oxide baseline subtracted Raman spectra.

2.3.3. Gaussian peak deconvolution

A gaussian peak deconvolution software package based on python's lmfit module was used to deconvolute the peak positions for the baseline subtracted W oxide Raman signal. The Levenberg-Marquardt algorithm, a damped least-squares (DLS), was used in combination with a BIC statistic to determine the most likely number of gaussian peaks and their parameters (peak position, FWHM and amplitude) which form up the tested spectra. Gaussian functions were chosen to fit the underlying spectra as is typical for solids with $\tau_a >> \tau_c$, where τ_a is the lifetime of the vibrationally excited bond and τ_c is the de-phasing lifetime. The low ampltidue of lattice vibrations in tungsten at low temperatures ensures that the de-phasing lifetime is small [38]. Fig. 4 illustrates the deconvolution process on an example W oxide Raman spectra.

2.4. Oxidation procedure

In this work, oxidation at a relatively low temperature was considered to make the set-up easier: $T = 400$ °C – close to the conditions used by Schlueter & Balden [24]. Under these conditions, interaction between W and the crucible material can be ignored. Because oxidation is slow compared to the chamber filling time, the oxygen partial pressure or the oxidation time can be efficiently varied to model specific oxidation stages. In addition, $T = 400$ °C corresponds to the starting conditions of a W divertor monoblock during LOCA, as simulated in [39].

Each sample (a full list of samples with respective experimental conditions is given in Table 1) was placed in Al_2O_3 crucibles with 0.12 ml capacity, polished side facing upwards. No lid was used to cover the samples. The crucibles were then placed on top of the Pt heating stage with Pt/Pt-Rh sensors of a Linseis STA PT1600 simultaneous thermal analyser. The chamber was then evacuated and samples heated up to 400 °C with an initial heating rate 20 deg./min which was changed half-way through the heating process to 10 deg./min (Fig. 5a) to decrease thermal inertia. After thermal equilibration, the instrument chamber was filled with Ar–20 % O_2 at a flow rate 38 l/h. Isothermal oxidation segments

Table 1: A list of samples with respective oxidation conditions

No.	Partial pressure of Ar–20% O_2 (bar)	Oxidation time (h)	Comments
1	0.01	1/3	
2	0.05		
3	0.07		
4	0.10		
5	0.13		
6	0.15		
7	0.18		
8	0.20		
10	1		#2, re-oxidized
11		1	#5, re-oxidized
12		5	No EBSD data
13		10	No EBSD data
14		72	#1, re-oxidized

were designed differently to model:

(a) *Initiation of oxidation.* Chamber was filled up to different oxygen partial pressures below 1 bar. The oxidation time was kept at 20 mins (Fig. 5b), which is much longer than the transient period when the gas was flowing in or out. Different initial stages of oxidation could be observed depending on the controlled atmosphere inside the chamber;

(b) *Progression of oxidation.* Pressure was kept at 1 bar during the whole duration of oxidation. Oxidation time varied from 20 min to 72 h.

The chamber was then evacuated and the furnace cooled down to room temperature at 20 deg./min.

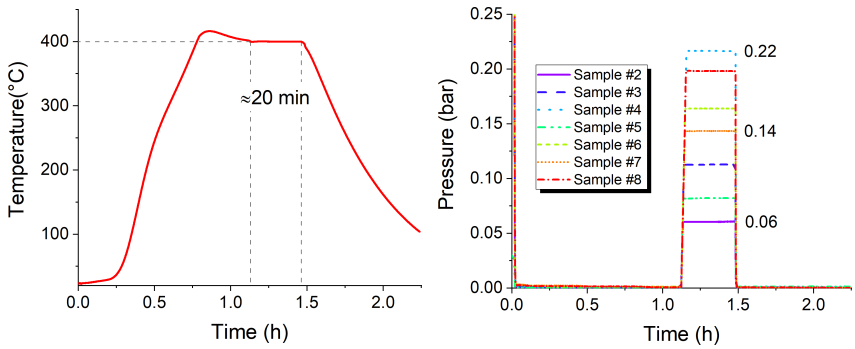

(a) (b)

Figure 5: Oxidation conditions in the STA: (a) time-temperature profile (measured values); (b) Ar–20%O_2 partial pressure profile (measured values).

3. Results and Discussion

3.1. Summary of reference spectra

A well-developed Raman peak database for characterisation of tungsten oxides doesn't exist. Therefore, reference samples of WO_3 (Tungsten (VI) oxide) and WO_2 (Tungsten (IV) oxide) powders were purchased from Sigma-Aldrich and characterised with Raman scattering analysis. It was noticed that WO_2 was unstable at a laser power $W > 4$ mW. The instability also manifested itself as an irreversible change of color from black to blue-violet. Different polymorphous states of WO_3 which were not readily available for purchase were analysed by digitalising published literature and subjecting them to the same baseline subtraction, smoothing and peak fitting as described in Sect. 2.3. Individual positions of the peaks were additionally confirmed by a Fourier self-deconvolution procedure [40]. The resulting spectral shapes are provided in Fig. 6, and Table 2 lists all the peak positions arranged so that the reader is easily able to match the occurrence of a specific peak to particular oxide phases.

Referring to Fig. 6, a few discrepancies between digitised literature spectral data are observed and this might be attributed to different instrumental settings. Hence, where possible, measurement conditions were kept to as described in the experimental procedure outlined in Sect. 2.2.2. The low-wavenumber

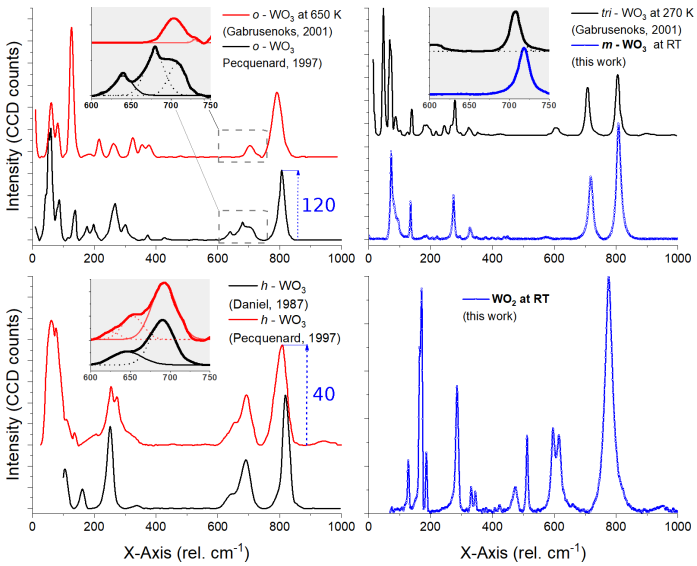

Figure 6: Raman spectra for a variety of crystalline tungsten oxides: hexagonal WO_3 ($h-WO_3$) [41, 42]; orthorhombic WO_3 ($o-WO_3$) [41, 43]; monoclinic WO_3 ($m-WO_3$); triclinic WO_3 ($tri-WO_3$) [41]; and monoclinic WO_2.

region of Table 2 shows that only few peaks can be used as markers of the oxide phase – especially when the signal/noise ratio is weak. In addition, bands below 200 cm^{-1} can be ascribed to lattice vibrations according to [44]. Therefore, the 600–1000 cm^{-1} region of the spectra is used for phase analysis, as the spacing between characteristic peaks for different oxides phases seems to be sufficient for robust peak deconvolution. All the analysed Raman spectra of W oxides exhibit a dominant peak in the range $770 - 820$ cm^{-1}. Because non-oxidized tungsten does not show any significant Raman signal (perhaps, only fluorescence, which contributes to the baseline), a sum filter in the range $750 - 850$ cm^{-1} may be used as an indicator of the thickness of an oxide scale grown on W metal. Additional examination of the reference spectra shows that at the same experimental conditions (i.e., laser power, spectrometer configuration, etc.), the Raman signal of certain oxide phases is inherently weaker than of the others (Fig. 6). This is a key factor contributing to the occurrence of 'tails' and 'humps' on the measured Raman spectral peaks.

Table 2: Results of peak deconvolution for all reference Raman spectra. Peak positions of major peaks are highlighted in bold. Grey rectangles outline the footprint peaks characteristic to a specific phase. Long dash indicates no data is available for this spectral position. Empty space means absence of peak.

Peak positions (cm^{-1})						
WO_2	*tri* -**WO_3**	*m* -**WO_3**	*o* -**WO_3**		*h* -**WO_3**	
this work	[41]	*this work*	at 650 K [41]	at RT [43]	[42]	[43]
—	**47**			43	—	**46***
—				**52**	—	**52***
—			**61**	**59**	—	**61***
75	**70**	**73**			—	
	87		**82**	84	—	**80***
	102					
			118	116	106	116
128	125	123	**126**			
	139	**135**		**134***		137
				140*		
165*					**161**	
171*				176		
186	186	184	185			
				199		200
	218	216	217			
	245				247	
					253	**254***
	263		263	**265**		
285	**278**	**274**				**275***
	296			301		
330	324	329	325		336	
345	352		354			
			377	373		
423	423			429		

Table 2 continued from previous page

Peak position (cm^{-1})						
WO_2	*tri* **-WO_3**	*m* **-WO_3**	*o* **-WO_3**		*h* **-WO_3**	
473			479			
512						
		574				
595	**606**					
615						625
660				640	646	653
696				**680**	**690**	**692**
	708	**718**	704	708		
			730			
777						784
	805	**808**	**791**	**807**	**820**	**810**
			834			
950						946

* Multiple overlaid peaks

3.2. Initiation and growth: correlating EBSD and Raman scattering maps

First results were gathered for the variable p_{Ar-O_2} oxidation runs with a 20 min duration (Table 1). Then the samples were exposed to oxygen at normal pressure while the oxidation time was allowed to vary up to 72 h (Sect. 2.4).

The results of applying the sum spectral filter (770–820 cm^{-1}) to the Raman spectral data gathered for a 75 μm $\times$ 75 μm region on the less-oxidised samples are shown in Fig. 7. A clear preference is observed for oxidation on {1 1 1} oriented W grains compared to {0 0 1} type orientations. This was noticed for all samples in the initiation stage (p_{Ar-O_2} = 0.01–0.2 bar).

This reduction of intensity in the Raman signal for {0 0 1} and {1 1 1} type surface grain orientations, used as an indicator for oxide thickness, is shown in Fig. 8, and this presents direct evidence of a thinner oxide on {0 0 1} planes.

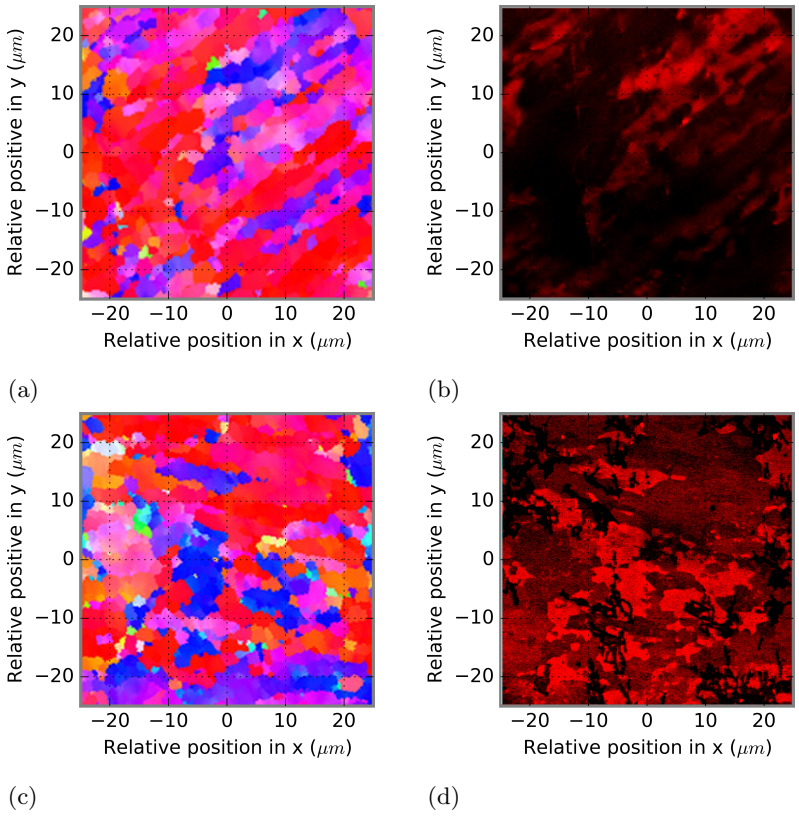

Figure 7: Exact overlays of the EBSD IPF z map (left column) and the intensity map of the principal ν(O – W – O) Raman peak (right column) for short oxidation: (a) and (b) – Sample 4 ($p_{\mathrm{Ar-O_2}} = 0.1$ bar); (c) and (d) – Sample 8 ($p_{\mathrm{Ar-O_2}} = 0.2$ bar).

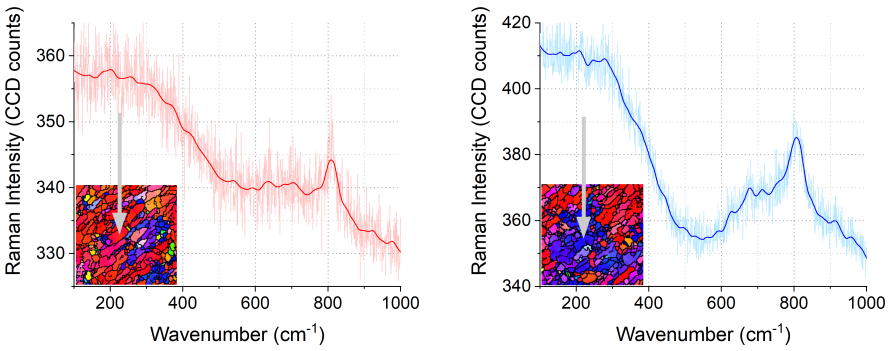

(a) (b)

Figure 8: Characteristic Raman spectra of the oxide layer grown on Sample 4 ($p_{\mathrm{Ar-O_2}}$ = 0.1 bar) at the surfaces of two W grains with different crystallographic orientations: (a) {0 0 1} oriented; (b) {1 1 1} oriented.

Schlueter & Balden [24] observed that the {1 1 1} oriented W grains showed a lower oxidation rate compared to the {0 0 1} orientations, e.g. at 600 °C for 30 min or at 450 °C for 96 h. At first, this seems to contradict the results discussed above as the preference observed in this work is opposite.

For the next stage, the same spectral analysis was applied to the Raman data gathered from samples oxidised at normal pressure for 20 min, 1 h, 5 h, 10 h and 72 h. The results for two samples exposed to oxygen for 20 min and 72 h are shown in Fig. 9. In these cases, the preference on {1 1 1} type orientations grows weaker with longer oxidation time. After 72 h of oxidation, the oxide grown on the {0 0 1} type orientations appears to show a more intense Raman signal. This was the same result which was obtained by Schlueter & Balden [24]. The oxide growing on the {0 0 1} oriented grains is thicker, hence the oxide scale on the {0 0 1} oriented grains grows faster than for the {1 1 1} orientation – when the oxide is thicker than at short oxidation runs.

3.3. Tungsten oxide phase analysis

From the EBSD map for Sample 4 ($p_{\mathrm{Ar-O_2}}$ = 0.1 bar) and Sample 8 ($p_{\mathrm{Ar-O_2}}$ = 0.2 bar), 2 × 25 points were selected corresponding to original tungsten grains

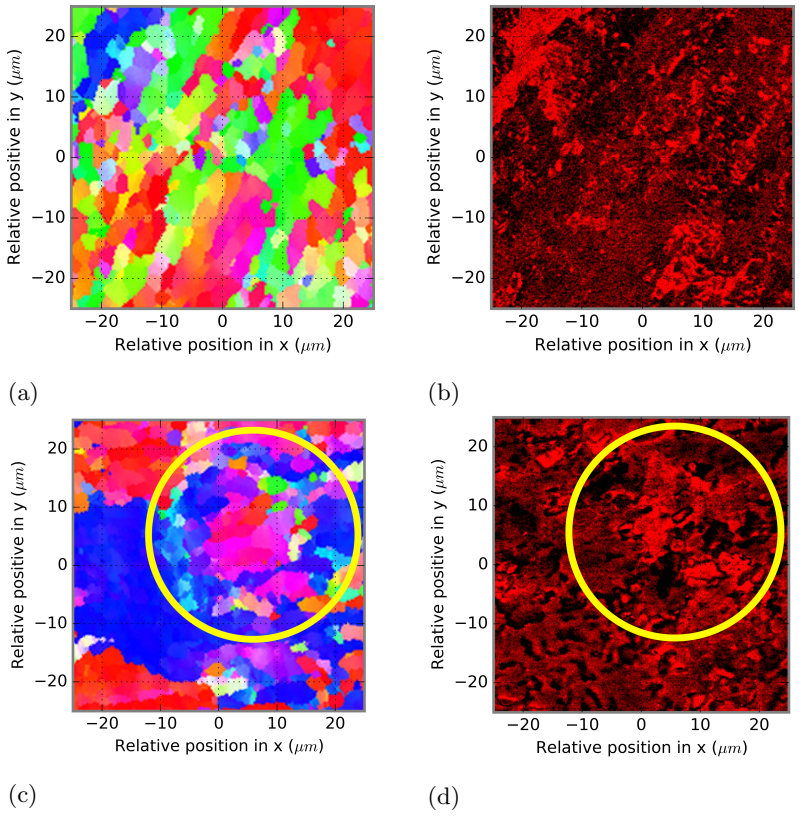

Figure 9: Exact overlays of the EBSD IPF z map (left column) and the intensity map of the principal ν(O – W – O) Raman peak (right column): (a) and (b) – Sample 9 (20 mins); (c) and (d) – Sample 13 (72 h).

of $\{0\,0\,1\}$ and $\{1\,1\,1\}$ type orientation for subsequent Raman analysis. The statistical average of the Raman spectra corresponding to different orientations was calculated. The averaged spectra corresponding to each orientation are shown in Fig. 10. For oxides grown on W grains oriented on $\{0\,0\,1\}$ at different partial pressures, a shift in the local maximum is observed. This shift in peak from 690 cm^{-1} towards 710 cm^{-1} is characteristic to a phase transformation from h–WO_3 to o–WO_3. Furthermore, the amplitude of the dominant 806 cm^{-1} peak above the baseline for $\{0\,0\,1\}$ type orientation increases by a much larger factor than for the $\{1\,1\,1\}$ type orientation. The peak shift is not observed on $\{1\,1\,1\}$ orientation either. Referring to Fig. 6, the amplitude of the o–WO_3 806 cm^{-1} peak is three times the amplitude of the corresponding h–WO_3 peak. For the $\{0\,0\,1\}$ type orientation, the presence of the shift in local maxima combined with the pronounced increase in intensity of the Raman signal is a strong indicator of a phase transformation. To verify this, the averaged spectra for each orientation in Samples 4 and 8 were passed through the deconvolution procedure outlined in Sect. 2.3. The results of deconvolution (Fig. 11) showed a difference not only in the number of peaks but also in peak positions. The $\{0\,0\,1\}$ type orientation Raman spectra was calculated to compose of two peaks at 636 cm^{-1} and 690 cm^{-1}, which referring to Table 2 matches up well with the hexagonal tungsten oxide (h–WO_3). Conversely, the oxide Raman spectra on W grains with $\{1\,1\,1\}$ type orientation was calculated to compose of three peaks at positions 643 cm^{-1}, 676 cm^{-1} and 702 cm^{-1}. Again referring to Table 2, these positions match up well with the orthorhombic tungsten oxide o–WO_3. For Sample 8, the deconvolution procedure showed that both $\{0\,0\,1\}$ and $\{1\,1\,1\}$ orientations grow an o–WO_3 type oxide, with three distinct peaks detected in the range $639 - 645$ cm^{-1}, $676 - 681$ cm^{-1} and $702 - 703$ cm^{-1}.

The formation of metastable h–WO_3 on $\{0\,0\,1\}$ type grains might explain the sluggish growth during the onset of oxidation. The Gibbs free energy cost of its formation relative to the thermodynamically stable o–WO_3 phase [45] scales with the thickness of the oxide and acts to decrease the stability of the h–WO_3 during growth. It is possible that the h–WO_3 phase forms preferentially

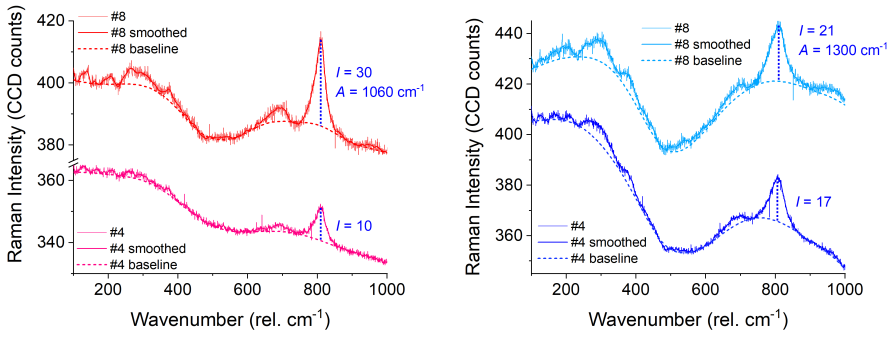

(a) (b)

Figure 10: Averaged Raman spectra over 25 selected regions corresponding to different tungsten surface grain orientations for Sample 4 ($p_{\mathrm{Ar\text{-}O_2}} = 0.1$ bar) and Sample 8 ($p_{\mathrm{Ar\text{-}O_2}} = 0.2$ bar): (a) – oxides on {1 0 0} tungsten grains; (b) – oxides on {1 1 1} tungsten grains. The intensity I of the main peak and its area A [cm^{-1}] are shown alongside the corresponding spectra.

on W grains oriented on {0 0 1} because of a lower crystal structure mismatch and/or favourable bonding compared to o–WO_3, thereby reducing the effective interfacial energy of the h–WO_3 bulk relative to o–WO_3 bulk interface. However, this negative interfacial energy is independent of the oxide thickness and therefore, the initial reduction in free energy costs is outweighed as the oxide grows thicker. This might explain why the h–WO_3 grows unstable at a certain thickness, transforming to the stable o–WO_3 phase.

However, the h–WO_3 to o–WO_3 transformation does not explain the more rapid growth of the o–WO_3 phase on {0 0 1} grain orientations at the late oxidation stages. For oxidation runs longer than 1 h, a colour change from yellow to blue to purple was observed (Fig. 12). The moment of this colour change seems to coincide with the observed reversal in preferential oxidation. Therefore, it is inferred that this colour change is attributed to a separate phase transformation to an entirely different oxide, and these new coloured oxides might contain valuable information into the reason for the reversal of preferential oxidation.

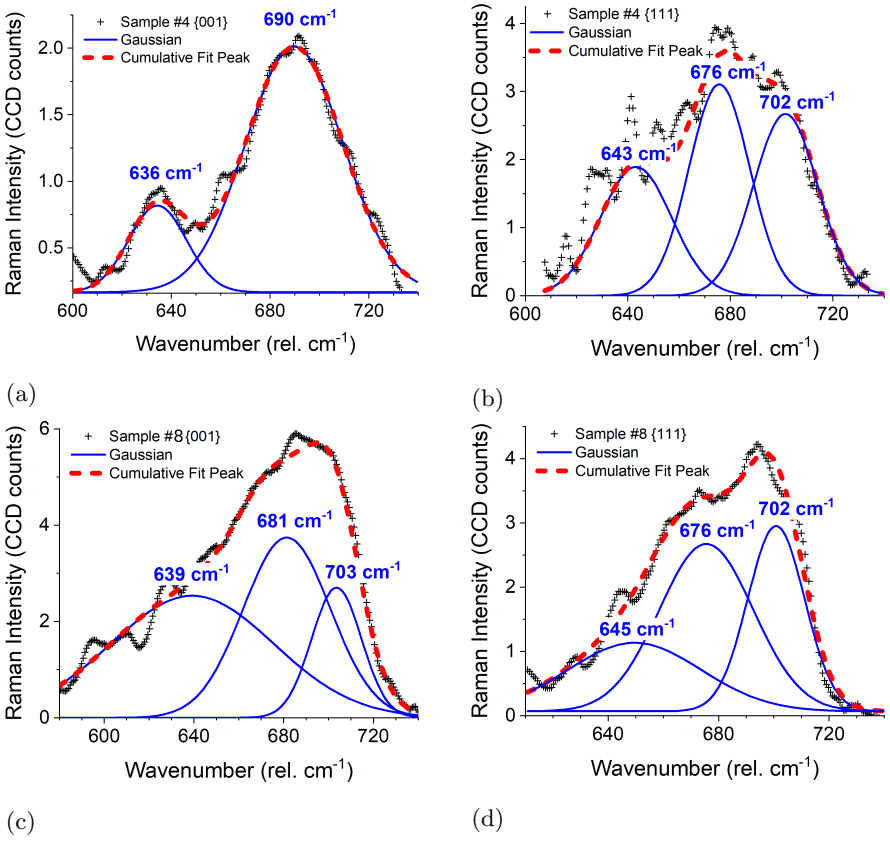

Figure 11: De-convoluted peak positions for {0 0 1} (left column) and {1 1 1} (right column) type grain orientations sampled over a $350 - 350$ μm region for: (a) and (b) – Sample 4 ($p_{\text{Ar-O}_2} = 0.1$ bar); (c) and (d) – Sample 8 ($p_{\text{Ar-O}_2} = 0.2$ bar).

3.4. Correlating EBSD and confocal topography maps

As outlined in Sect. 2.2.1 and shown in Fig. 2, preferential polishing of softer W grains corresponding to {1 1 1} type surface orientation generates a surface topography which matches well with EBSD mapping. However, it was observed that the variation in topography as characterised by the interquartile range (IQR) initially decreases. This indicates that valley regions in the topography, which correspond to {1 1 1} type orientations initially grow more rapidly. This is in agreement with Fig. 7. However, for longer oxidation times, the variation of topography begins to increase again. This indicates that oxidation on W grains protruding from the surface and showing {0 0 1} type orientations becomes dominant over the low-lying {1 1 1} regions. This is again in agreement with the transition in the Raman signal intensity seen in Fig. 9. The increase in variation of topography for long oxidation times can be seen in Fig. 12, which shows a doubling in the surface roughness between 1 h to 72 h oxidation and is another separate source of evidence in support of this preferential oxidation mechanism.

4. Conclusion

Short exposures of fusion grade tungsten to oxygen during abnormal operation or accidental conditions lead to preferential oxidation of tungsten grains oriented on either {1 1 1} or {0 0 1} crystallographic planes. When the oxide is thin, it forms preferentially on {1 1 1} oriented tungsten grains. According to currently published research, oxidation on {1 1 1} tungsten planes is reported to be the slowest, which at first seems contradictory. However, longer oxidations at normal pressure (up to 72 h) showed a reversal in the initial preferential oxidation from {1 1 1} to {0 0 1}, which was confirmed by Raman scattering and topography analysis. Hence, it can be inferred that the crystallographic preference of oxidation changes with time.

A robust method for smoothing, baseline subtraction and deconvolution based on a statistical information criterion was adopted to analyse the Raman

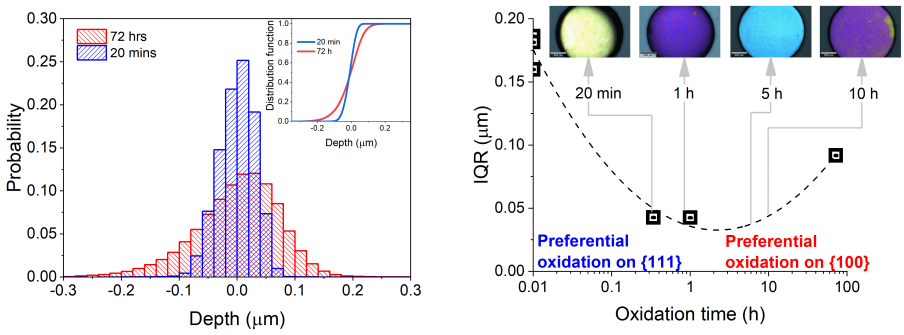

(a) (b)

Figure 12: Results of CLSM image processing showing: (a) the distribution of relative surface height in tungsten samples oxidised for 20 min and 72 h; (b) evolution of interquartile range (IQR) of surface roughness from as-polished tungsten, through oxide initiation to growth, showing an initial drop in topography and subsequent increase. It is inferred that the minimum of IQR corresponds to reversal of oxidation preference from {1 1 1} to {0 0 1} tungsten planes.

scattering response of these oxides. Using this method, the metastable h–WO_3 phase was shown to form specifically on {0 0 1} oriented tungsten grains just at the start of oxidation and is later either substituted or covered by an o–WO_3 oxide layer. Tungsten grains with a {1 1 1} surface orientation showed only the orthorhombic phase both at the initiation and progression stages of oxidation.

It is still currently unclear what drives the rapid growth of tungsten oxide on {0 0 1} tungsten planes. The reversal in preferential oxidation coincides with an oxide colour change from yellow to blue to purple, and it is expected that a second phase transformation holds the answer to why this happens. Further work will involve the analysis of the composition and structure of this coloured oxide.

Acknowledgements

This work was funded by the RCUK Energy Programme (Grant No. EP/P012450/1). The research used UKAEA's Materials Research Facility, which has been funded

by and is part of the UK's National Nuclear User Facility and Henry Royce Institute for Advanced Materials. The authors would like to thank Mr. Christopher Smith for his help in configuring the first Raman measurements and for valuable suggestions used to drive this work further.

Data availability

The raw/processed data required to reproduce these findings is stored in a dropbox repository and may be shared on request by contacting the corresponding author. Due to technical limitations, it is not possible to upload all data to a public repository. A software toolkit implementing the methodology described for data processing in this work is available at `https://github.com/gfulton96/W_Oxidation`.

References

[1] Habainy, J. et al, Thermal diffusivity of tungsten irradiated with protons up to 5.8 dpa, Journal of Nuclear Materials 509 (2018) 152 – 157. doi:https://doi.org/10.1016/j.jnucmat.2018.06.041.

[2] Davis, J. et al, Assessment of tungsten for use in the ITER plasma facing components, Journal of Nuclear Materials 258-263 (1998) 308 – 312. doi:https://doi.org/10.1016/S0022-3115(98)00285-2.

[3] Nishijima, D. et al, Sputtering properties of tungsten 'fuzzy' surfaces, Journal of Nuclear Materials 415 (1, Supplement) (2011) S96 – S99, proceedings of the 19th International Conference on Plasma-Surface Interactions in Controlled Fusion. doi:https://doi.org/10.1016/j.jnucmat.2010.12.017.

[4] Voitsenya, V. et al, Effect of sputtering on self-damaged ITER-grade, Journal of Nuclear Materials 453 (1) (2014) 60 – 65. doi:https://doi.org/10.1016/j.jnucmat.2014.06.037.

[5] Pitts, R. et al, A full tungsten divertor for ITER: Physics issues and design status, Journal of Nuclear Materials 438 (2013) S48 – 556, proceedings of the 20th International Conference on Plasma-Surface Interactions in Controlled Fusion Devices. doi:https://doi.org/10.1016/j.jnucmat.2013.01.008.

[6] Hirai, T. et al, Status of technology r&d for the ITER tungsten divertor monoblock, Journal of Nuclear Materials 463 (2015) 1248 – 1251, plasma-surface interactions 21. doi:https://doi.org/10.1016/j.jnucmat.2014.12.027.

[7] Perkins, R.A. and Crooks, D.D., Low-pressure, high-temperature oxidation of tungsten, JOM 13 (7) (1961) 490–493. doi:10.1007/BF03378089.

[8] Cifuentes, S., Monge, M. and Pérez, P., On the oxidation mechanism of pure tungsten in the temperature range 600–800 °C, Corrosion Science 57 (2012) 114 – 121. doi:https://doi.org/10.1016/j.corsci.2011.12.027.

[9] Hirai, T. et al, Use of tungsten material for the ITER divertor, Nuclear Materials and Energy 9 (2016) 616 – 622. doi:https://doi.org/10.1016/j.nme.2016.07.003.

[10] Orchard, J., Peacock, A. and Saibene, G., JET experience in recovery from large air leak incidents, Journal of Nuclear Materials 200 (3) (1993) 395 – 399. doi:https://doi.org/10.1016/0022-3115(93)90316-Q.

[11] Ebert, E. and Raeder, J., LOCA, LOFA and LOVA analyses pertaining to JET/ITER safety design guidance, Fusion Engineering and Design 17 (1991) 307 – 312. doi:https://doi.org/10.1016/0920-3796(91)90074-Z.

[12] Tillack, M. et al, The use of water in a fusion power core, Fusion Engineering and Design 91 (2015) 52 – 59. doi:https://doi.org/10.1016/j.fusengdes.2014.12.013.

[13] Smolik, G.R., Piet, S.J. and Jr., R.M.N., Predictions of radioactive tungsten release for hypothetical ITER accidents, Fusion Technology 19 (3P2B) (1991) 1398–1402. doi:10.13182/FST91-A29538.

[14] Wurster, S. et al, Recent progress in R&D on tungsten alloys for divertor structural and plasma facing materials, Journal of Nuclear Materials 442 (1, Supplement 1) (2013) S181 – S189, Fifteenth International conference on fusion reactor materials. doi:https://doi.org/10.1016/j.jnucmat.2013.02.074.

[15] Litnovsky, A. et al, Advanced smart tungsten alloys for a future fusion power plant, Plasma Physics and Controlled Fusion 59 (6) (2017) 064003. doi:10.1088/1361-6587/aa6948.

[16] Klein, F. et al, On oxidation resistance mechanisms at 1273 K of tungsten-based alloys containing chromium and yttria, Metals 8 (7). doi:10.3390/met8070488.

[17] Litnovsky, A. et al, New oxidation-resistant tungsten alloys for use in the nuclear fusion reactors, Physica Scripta T170 (2017) 014012. doi:10.1088/1402-4896/aa81f5.

[18] Li, Y. et al, The hot forging behaviour and its effects on the oxidation behaviour of W–Cr alloy, Corrosion Science 83 (2014) 367 – 374. doi:https://doi.org/10.1016/j.corsci.2014.03.005.

[19] Lee, D.B. and Simkovich, G., Oxidation of Mo–W–Cr–Pd alloys, Journal of the Less Common Metals 163 (1) (1990) 51 – 62. doi:https://doi.org/10.1016/0022-5088(90)90085-X.

[20] Lee, D.B. and Simkovich, G., Oxidation resistant Mo–W–Cr–Pd alloys with palladium coatings, Journal of the Less Common Metals 169 (1) (1991) 19 – 23. doi:https://doi.org/10.1016/0022-5088(91)90231-R.

[21] Litnovsky, A. et al, Smart first wall materials for intrinsic safety of a fusion power plant, Fusion Engineering and Design 136 (2018) 878 – 882, special

Issue: Proceedings of the 13th International Symposium on Fusion Nuclear Technology (ISFNT-13). doi:https://doi.org/10.1016/j.fusengdes.2018.04.028.

[22] Gludovatz, B. et al, Fracture toughness of polycrystalline tungsten alloys, International Journal of Refractory Metals and Hard Materials 28 (6) (2010) 674 – 678, selected papers of the 17th International Plansee Seminar 2010 in Reutte, Austria: Tungsten and Molybdenum. doi:https://doi.org/10.1016/j.ijrmhm.2010.04.007.

[23] Sikka, V. and Rosa, C., The oxidation kinetics of tungsten and the determination of oxygen diffusion coefficient in tungsten trioxide, Corrosion Science 20 (11) (1980) 1201 – 1219. doi:https://doi.org/10.1016/0010-938X(80)90092-X.

[24] Schlueter, K. and Balden, M., Dependence of oxidation on the surface orientation of tungsten grains, International Journal of Refractory Metals and Hard Materials 79 (2019) 102 – 107. doi:https://doi.org/10.1016/j.ijrmhm.2018.11.012.

[25] Gulbransen, E. and Andrew, K., Kinetics of the oxidation of pure tungsten from 500 to 1300 °C, Journal of the Electrochemical Society 107 (7) (1960) 619–628.

[26] Lee, C.M. and Sohn, D.S., Enhanced high-temperature oxidation resistance of a zirconium alloy cladding by high-temperature preformed oxide on the cladding, Corrosion Science 131 (2018) 116 – 125. doi:https://doi.org/10.1016/j.corsci.2017.11.019.

[27] Zhao, Q. et al, Preferential oxidation of intermetallic compounds in Ag–2Sn–4La alloy, Corrosion Science 143 (2018) 177 – 186. doi:https://doi.org/10.1016/j.corsci.2018.08.017.

[28] Wriedt, H.A., The O–W (oxygen-tungsten) system, Bulletin of Alloy Phase Diagrams 10 (4) (1989) 368–384. doi:10.1007/BF02877593.

[29] English, J., Binary and ternary phase diagrams of columbium, molybdenum, tantalum, and tungsten, Tech. rep., Battelle memorial institute, Columbus Ohio. The defense materials information center (1961).

[30] Santato, C., Ulmann, M. and Augustynski, J., Photoelectrochemical properties of nanostructured tungsten trioxide films, The Journal of Physical Chemistry B 105 (5) (2001) 936–940. doi:10.1021/jp002232q.

[31] Chou, J.C. and Chiang, J.L., Ion sensitive field effect transistor with amorphous tungsten trioxide gate for pH sensing, Sensors and Actuators B: Chemical 62 (2) (2000) 81 – 87. doi:https://doi.org/10.1016/S0925-4005(99)00363-9.

[32] Balaji, S. et al, Micro-Raman spectroscopic characterization of a tunable electrochromic device for application in smart windows, Journal of Raman Spectroscopy 40 (1) (2009) 92–100. doi:10.1002/jrs.2086.

[33] Addab, Y. et al, Formation of thin tungsten oxide layers: characterization and exposure to deuterium, Physica Scripta T167 (2016) 014036. doi:10.1088/0031-8949/t167/1/014036.

[34] Hijazi, H. et al, Tungsten oxide thin film exposed to low energy He plasma: Evidence for a thermal enhancement of the erosion yield, Journal of Nuclear Materials 484 (2017) 91 – 97. doi:https://doi.org/10.1016/j.jnucmat.2016.11.030.

[35] Kiselev, R. et al, Design and first applications of a flexible Raman microspectroscopic system for biological imaging, Biomedical Spectroscopy and Imaging 5 (2) (2016) 115–127.

[36] He, S. et al, Baseline correction for Raman spectra using an improved asymmetric least squares method, Anal. Methods 6 (2014) 4402–4407. doi:10.1039/C4AY00068D.

[37] Eilers, P.H. and Boelens, H.F., Baseline correction with asymmetric least squares smoothing, Leiden University Medical Centre Report 1 (1) (2005) 5.

[38] Bradley, M.S., Lineshapes in IR and Raman spectroscopy: A primer, Spectroscopy 30 (11) (2015) 42–46.

[39] Maisonnier, D. et al, DEMO and fusion power plant conceptual studies in europe, Fusion Engineering and Design 81 (8) (2006) 1123 – 1130, proceedings of the Seventh International Symposium on Fusion Nuclear Technology. doi:https://doi.org/10.1016/j.fusengdes.2005.08.055.

[40] Tooke, P., Fourier self-deconvolution in IR spectroscopy, TrAC Trends in Analytical Chemistry 7 (4) (1988) 130 – 136. doi:https://doi.org/10.1016/0165-9936(88)87010-9.

[41] Gabrusenoks, J. et al, Infrared and Raman spectroscopy of WO_3 and $CdWO_4$, Electrochimica Acta 46 (13) (2001) 2229 – 2231. doi:https://doi.org/10.1016/S0013-4686(01)00364-4.

[42] Daniel, M. et al, Infrared and Raman study of WO_3 tungsten trioxides and $WO_3 \cdot xH_2O$ tungsten trioxide hydrates, Journal of Solid State Chemistry 67 (2) (1987) 235 – 247. doi:https://doi.org/10.1016/0022-4596(87)90359-8.

[43] Pecquenard, B. et al, Orthorhombic WO_3 formed via a Ti-stabilized $WO_3 \cdot 13H_2O$ phase, Journal of Solid State Chemistry 135 (1) (1998) 159 – 168. doi:https://doi.org/10.1006/jssc.1997.7618.

[44] Djaoued, Y., Subramanian, B. and Brüning, R., Electrochromic devices based on porous tungsten oxide thin films, Journal of Nanomaterials 2012. doi:10.1155/2012/674168.

[45] Cazzanelli, E., Low-temperature polymorphism in tungsten trioxide powders and its dependence on mechanical treatments, Journal of Solid State Chemistry 143 (1999) 24 – 32.